Journal of Materials Chemistry A

ROYAL SOCIETY OF CHEMISTRY

PAPER

View Article Online
View Journal

Cite this: DOI: 10.1039/d0ta05655c

Enhanced photocatalysis by light-trapping optimization in inverse opals

Xiwen Zhang and Sajeev John*

Inverse opal photonic crystals with opal spheres of small diameters in the range of 70 to 170 nm have been widely adopted to enhance photocatalytic efficiency near the TiO_2 conduction band, using the slow-light modes on the red (long-wavelength) and blue (short-wavelength) edges of the fundamental optical stop gap. We show that these two spectral regions have comparable light harvesting abilities, but neither of them are the optimum spectral range for photocatalysis in TiO_2. Instead, the ideal resonant photonic modes are distributed among the higher order 5th to 15th photonic bands. By using larger opal spheres of ~380 nm diameter, to place these higher order slow-light modes into the visible spectrum of 400 to 550 nm in lightly doped anatase TiO_2, enhanced photocatalytic efficiency is possible. For an imaginary part of the dielectric constant 0.01, the maximum achievable photocurrent density reaches 2.09 mA cm^{-2} for a 6-layer inverse opal placed on a mirror substrate. This is 5.6 times the photocatalytic response of blue-edge slow photons near the TiO_2 electronic band edge.

Received 6th June 2020
Accepted 24th August 2020

DOI: 10.1039/d0ta05655c

rsc.li/materials-a

1 Introduction

Photocatalysis has a long and rich history with progressive research focus in the past few decades due in part to global issues of energy, environment, and public health. Improving solar photocatalytic efficiency is a key requirement for real-world applications such as hydrogen photoproduction, pollutant decontamination, and pathogen disinfection.[1–4] This involves efficient photogeneration of charge carriers from sunlight, separation and transport of electrons and holes to redox reaction centers on the surface of the catalyst.

Due to its strong photochemical activity, high stability and noncorrosiveness in solution, environmental and biological safety, as well as cost effectiveness, TiO_2 remains one of the most promising photocatalysts for the large scale implementation. However, the solar photocatalytic efficiency of TiO_2 is critically limited by its wide electronic band gap of 3.1–3.6 eV (*i.e.*, 345–400 nm). Solar irradiance in the ultraviolet (UV) region contains one-sixth the number of photons as in the 400 to 550 nm spectral range. Strong modifications by extrinsic doping can make TiO_2 more absorptive in the visible range, but its carrier transport can then be degraded by concomitant defect sites that act as deleterious electron–hole recombination centers.[5,6]

In this paper, we assume the TiO_2 is only lightly doped either intrinsically (by naturally occurring oxygen vacancies) or extrinsically so that the visible light absorptivity is nonvanishing but charge transport remains viable. We show that by optimizing the inverse opal (invop) structure *via* judicious choice of sphere diameter, lightly doped TiO_2 with weak intrinsic visible light absorptivity can nevertheless provide strong photogeneration of carriers. The mechanism for this enhanced absorption is wave-interference-based light trapping. This occurs through a broad and continuous spectral distribution of resonant slow-light modes that propagate more slowly and orthogonally to those surrounding the fundamental stop gap of the photonic crystal (PC).[7]

The invop PC [see Fig. 1(a)] is advantageous for certain types of photocatalysis because of its large internal surface area of contact with water. This exposes more reaction sites to chemical adsorbates, raising the volume reaction rate for heterogeneous catalysis. At the same time, light trapping boosts the charge carrier generation rate for the redox reaction.[8] The relevant PC photonic modes are said to support slow photons since their group velocities are much smaller than the speed of light in a homogeneous solid. This leads to long light–matter interaction for the generation of electron–hole pairs. Two types of slow-light modes have been considered in past experiments, associated with the lower and upper edges of the fundamental photonic stop gap [see Fig. 1(b)]. Photons on the long-wavelength edge are called "red-edge" slow-light and photons on the short-wavelength edge are called "blue-edge" slow-light.

Experimentally both the red-edge[8–11] and the blue-edge[10,12] slow photons have been aligned with the electronic band edges of the semiconductor catalysts or absorption bands of the sensitizers by choosing specific opal sphere diameters. However, there has been debate[13] whether the red-edge[8,14] or the blue-edge[15–17] modes are best for photocatalysis. Electromagnetic energy focuses more in the high refractive index material

Department of Physics and Astronomy, University of Toronto, 60 Saint George Street, Toronto, Ontario M5S 1A7, Canada. E-mail: john@physics.utoronto.ca

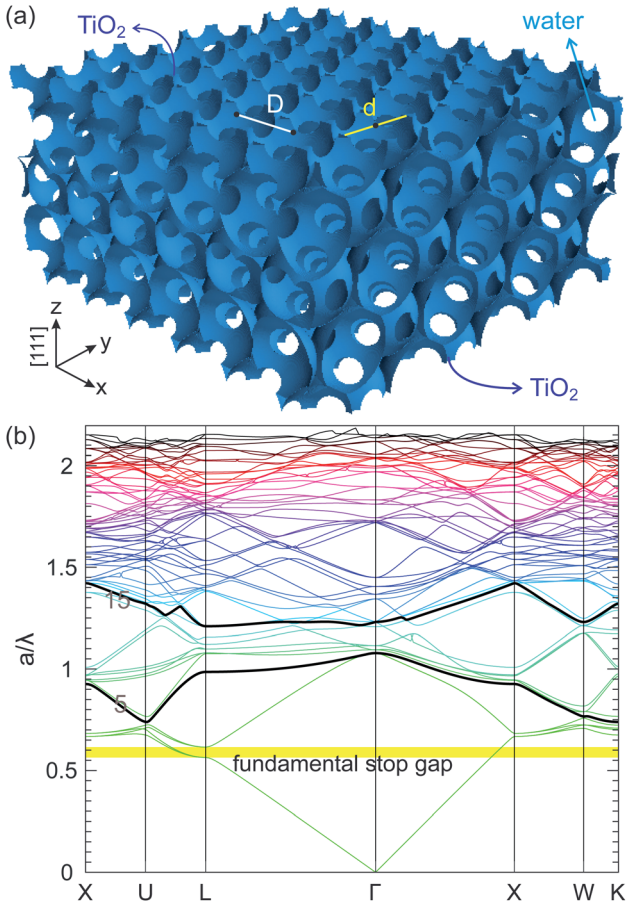

Fig. 1 Illustration of the invop PC. (a) The structure of the TiO_2 face-centered cubic invop PC with void diameter d and center-to-center distance D between adjacent voids. (b) The photonic band diagram of the invop PC immersed in water, with the refractive indices of the PC backbone and the void equal to $n_{TiO_2} = 2.25$ and $n_{H_2O} = 1.33$, respectively. The fundamental optical stop gap, surrounded by bands 1 and 2 below and bands 3 and 4 above, is marked by the yellow stripe. The optical bands 5 and 15, surrounding the most efficacious slow-light modes, are highlighted by the thick black lines.

(*i.e.*, the absorptive PC material) near the red edge of the stop gap, while it focuses more in the void near the blue edge. Nevertheless, the blue-edge slow-light modes dispense a significant fraction of energy in the PC backbone as well since the PC lattice constant is small compared with the wavelength of light.[18] When the red edge is aligned with the electronic band edge, the photonic stop gap appears to block light absorption just above the electronic band gap. However, the very short absorption length above the electronic band gap mitigates photonic stop gap reflection, which requires longer length scales to manifest.

We demonstrate that in a simplified model of frequency-independent absorption, red-edge slow photons are slightly better absorbed than blue-edge slow photons due to better overlap with the PC backbone. However, near the actual TiO_2 electronic band edge, the intrinsic absorptivity is strongly frequency-dependent. Consequently, blue-edge slow photons are slightly better absorbed than red-edge ones because the photonic stop gap does not block near-band-edge electronic transitions, and more photonic modes are involved in the light absorption. Overall, the blue-edge alignment (with the electronic band edge) marginally outperform red edge alignment, but neither edge of the fundamental stop gap exploits the light trapping potential available in inverse opals. Extensive experimental efforts[13,19,20] over the last 15 years have not discovered the superior capability of higher order photonic bands. This is due in part to the complexity of the materials with many sensitive variables, the challenge of accurate material fabrication, and the scarcity of relevant theoretical analysis.[18,19]

Our strategy involves identification of the best slow-light modes for light trapping and aligning these modes with electronic band tail transitions in TiO_2. We show that the PC modes between bands 5 and 15 enable 4.5–5 times light capture capability relative to previously studied red-edge and blue-edge slow-light modes. This is demonstrated in a model for TiO_2 in which band tail optical absorption is characterized by an imaginary part of the dielectric constant of 0.01. When the higher band slow-light modes are aligned with sub-gap electronic transitions in the 400 to 550 nm range, the maximum achievable photocurrent density [MAPD, see eqn (2)] reaches 2.09 mA cm^{-2} in a 6-layer invop PC deposited on a highly reflective substrate. This far exceeds the 0.37 mA cm^{-2} obtained using the traditional blue-edge slow-light strategy.

2 Figures of merit

The invop PC is characterized by the void diameter, d, equal to the original opal sphere diameter, the nearest neighbor voids' center-to-center distance D, and the number of opal layers n_L along the natural growth direction [111] defined by the coordinate z-axis [see Fig. 1(a) and App. A.2]. The lattice constant of this structure is $a = \sqrt{2}D$. Unless otherwise specified, we focus on invop PC of $n_L = 6$ opal layers (two unit cells), with $d = 1.0558D$, of which the original opal template can be prepared by self-assembly techniques such as the vertical deposition[21] and the confined assembly.[22] This gives rise to a feasible filling fraction (fraction of total volume occupied by TiO_2 backbone) of the PC $F = 15\%$ for $n_L \to \infty$ and $F = 18.79\%$ for $n_L = 6$. Similar filling fractions have been used in experiments and numerical simulations of invop PC enhanced photocatalysis.[23,24] The effect of increasing the number of opal layers is discussed in Sec. 4.2.

Anatase TiO_2 is chosen as the invop backbone since it demonstrates much higher photocatalytic activity than the rutile polymorph.[25,26] The invop photocatalyst is assumed to be immobilized on a support of fused silica (FS) or a perfect mirror (MR) in an aqueous background. The composite architectures are denoted as "invop-FS" and "invop-MR", respectively. Glass substrates are commonly adopted in photocatalysis and dye sensitized solar cell experiments, but as shown below, a highly reflective metal substrate is much more effective in light harvesting by closing the photon transmission channel.

Numerical simulations of optical absorptivities in the invop PC and bulk planar films are carried out by solving Maxwell's wave equation for x-polarized light under normal incidence

(unless otherwise specified) using the finite-difference time-domain (FDTD) method. As we are interested in broadband enhancement of optical absorption, an average absorptivity is defined as:

$$A_{\mathrm{avg}} = \frac{1}{f_1 - f_2}\int_{f_2}^{f_1} A(f)\mathrm{d}f, \tag{1}$$

where A is the absorptivity spectrum in the frequency range $[f_2, f_1]$. For the purpose of scaling, we express the frequency in terms of a/λ. Solar illumination assigns a spectral weight to each frequency component of the PC absorptivity. Accordingly, we define the maximum achievable photocurrent density (MAPD) in a wavelength region $[\lambda_1, \lambda_2]$ as:

$$\mathrm{MAPD} = \frac{e}{hc}\int_{\lambda_1}^{\lambda_2} A(\lambda)I_{\mathrm{s}}(\lambda)\lambda\mathrm{d}\lambda, \tag{2}$$

where e is the electron charge, h is the Planck constant, c is the speed of light in vacuum, and I_{s} is the AM1.5G solar irradiance spectrum. Although the current density may not be measured in some photocatalysis applications, MAPD is a valuable figure of merit for the optimization of the PC architecture by taking into account the light source intensity spectrum.

In both the average absorptivity and the MAPD, it is useful to quantify the PC light trapping efficacy by normalizing them to values obtained for an equivalent bulk planar TiO_2 film on FS support (denoted as "bulk-FS") of the same catalyst volume as the PC backbone. In this way we define two enhancement factors:

$$\beta = A_{\mathrm{avg}}^{\mathrm{PC}}/A_{\mathrm{avg}}^{\mathrm{bulk}}, \tag{3}$$

$$\zeta = \mathrm{MAPD}^{\mathrm{PC}}/\mathrm{MAPD}^{\mathrm{bulk}}. \tag{4}$$

3 Optimization of slow-light modes for light harvesting

We compare the light trapping abilities of various invop PC architectures using two separate models of the TiO_2 dielectric function. Model I is a dispersionless dielectric function, aimed to describe weak sub-gap electronic transitions, in which the dielectric constant $\varepsilon = \varepsilon' + i\varepsilon''$ is assumed to be frequency independent, where $\varepsilon' = 5.06$ and ε'' are the real and imaginary parts of the dielectric constant, respectively. Depending on the nature of doping, different values of ε'' are chosen. This simplified model allows the optimization of sub-gap light harvesting without inclusion of UV absorption where sunlight is weak and light-trapping is of little efficacy. It also enables the scaling property of Maxwell's wave equation, which generalizes our findings to different spectral regions by proportionally resizing the PC (see discussions in App. A.1 for details). In Model I, the light trapping ability is measured by the average absorptivity enhancement factor β over the spectrum $\lambda \in [400, 550]$ nm. In Sec. 4, we introduce a more comprehensive Model II that ascribes the experimentally measured values of the dielectric function of anatase TiO_2 over the UV spectrum[27] and appends a constant value $\varepsilon'' = 0.01$ for the subgap spectrum. In this case the overall MAPD is tabulated for various invop PC architectures. As a matter of nomenclature, we append the constant subgap value of ε'' to the model name. So for instance, Model I.01 denotes Model I with the choice $\varepsilon'' = 0.01$.

3.1 Red-edge and blue-edge slow light for weak enhancement

Previous literature on the three-dimensional PC-based photocatalysis has focused on the red-edge and blue-edge slow-light modes around the fundamental optical stop gap of the

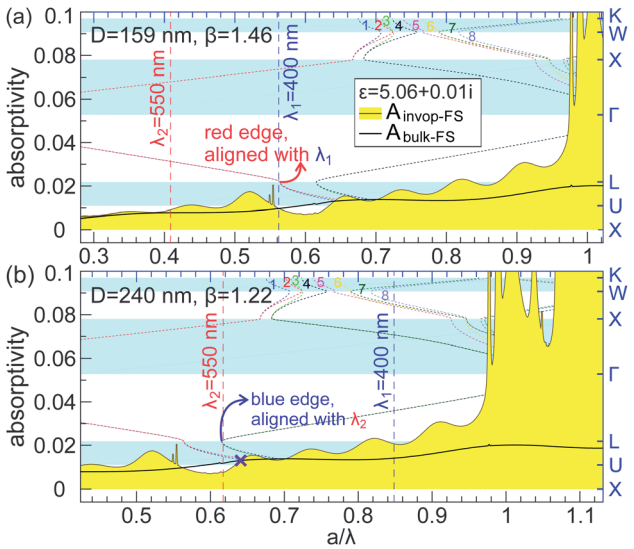

Fig. 2 The absorption spectra around the fundamental photonic stop gap of 6-layer invop-FS architectures (solid brown lines filled by yellow color) with (a) $D = 159$ nm, $d = 167.9$ nm, and (b) $D = 240$ nm, $d = 253.4$ nm, using the dispersionless dielectric Model I.01. The solid black lines depict absorptivities of planar bulk-FS structures of equivalent bulk thicknesses. The background short-dashed curves depict the photonic bands of the invop PC with the band numbers labeled. The vertical long-dashed lines demark the spectral region of interest. The thin purple cross indicates a specific frequency at which the absorptivities of the PC and the planar bulk anatase cross each other as a result of the fundamental photonic stop gap.

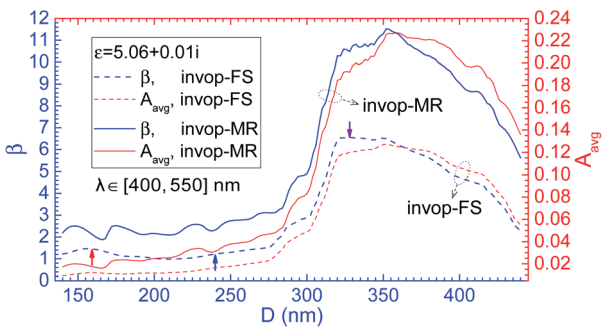

Fig. 3 The average absorptivity A_{avg} (red lines) and its enhancement factor β (blue lines) of a 6-layer invop PC on FS (dashed lines) and MR (solid lines) substrates as functions of D in the wavelength region of $\lambda \in [400, 550]$ nm for the dispersionless dielectric Model I.01. The red, blue and purple arrows correspond to Fig. 2(a), (b) and 4, respectively.

Table 1 Light harvesting figures of merit for different slow-light modes and their alignments to the TiO_2 electronic bands for a 6-layer inverse opal photonic crystal with opal diameter $d = 1.0558D$ and filling fraction $F = 18.79\%$ (15% for infinite-size crystal)

		Model I.01[a], $\lambda \in [400s, 550s]$ nm					Model II.01[b], $\lambda \in [282, 550]$ nm					
Photonic mode	Physical substrate	D (nm)	β	A_{avg}	ζ	MAPD[c]	Alignment to	D (nm)	β	A_{avg}	ζ	MAPD
Red-edge	FS	159s	**1.46**	0.012	1.41	0.096	TiO_2 band edge	70	1.20	0.262	**1.38**	0.202
Blue-edge	FS	250s	**1.30**	0.018	1.23	0.140	TiO_2 band edge	170	1.22	0.336	**1.39**	0.371
Higher order[d]	FS	328s	**6.55**	0.120	5.01	0.744	$\lambda \in [400, 550]$ nm	360	1.22	0.367	**3.31**	1.293
Higher order	MR	352s	**11.53**	0.226	10.52	1.691	$\lambda \in [400, 550]$ nm	380	1.42	0.429	**5.13**	2.087

[a] s is a scaling dimensionless constant varying from 0.87 to 1.3. The value of s is set to 1 for ζ and MAPD. [b] The visible range dielectric function is $5.06 + 0.01i$. [c] The unit of MAPD is mA cm^{-2}. [d] Higher order slow-light modes lie in between the 5th and the 15th photonic bands.

inverse opal structure. These appear in the 1st to 4th bands near the L-point in wave-vector space [see Fig. 1(b)]. To investigate these two edges, we place them in the frequency range of $\lambda \in [\lambda_1, \lambda_2]$ nm, where $\lambda_1 = 400$ nm and $\lambda_2 = 550$ nm, using two separate 6-layer invop PCs, one with $D = 159$ nm and the other with $D = 240$ nm as shown in Fig. 2(a) and (b), respectively. The dielectric function is from the dispersionless Model I.01 with $\varepsilon = 5.06 + 0.01i$.

When $D = 159$ nm, the red edge of the fundamental stop gap locates at $\lambda_1 = 400$ nm and the stop gap occurs in the near UV, resulting in an absorption enhancement factor of $\beta = 1.46$ in the [400, 550] nm wavelength range. When $D = 240$ nm, the blue edge of the fundamental stop gap locates at $\lambda_2 = 550$ nm and the stop gap occurs in an non-absorbing spectral region, giving rise to $\beta = 1.22$. Increasing the sphere size such that $D = 250$ nm places $\lambda_2 = 550$ nm at the purple cross in Fig. 2(b), causing $\beta = 1.3$. In either case, using Model I.01, the red edge of the fundamental photonic stop gap slightly outperforms the blue edge. This remains true for a wide variety of spectral ranges and larger number of opal layers (see discussions in App. B). The relatively small difference in β for the red- and blue-edge slow-light modes is explained by the similarity of their electromagnetic energy and Poynting vector distributions (see Fig. 13 in App. C).

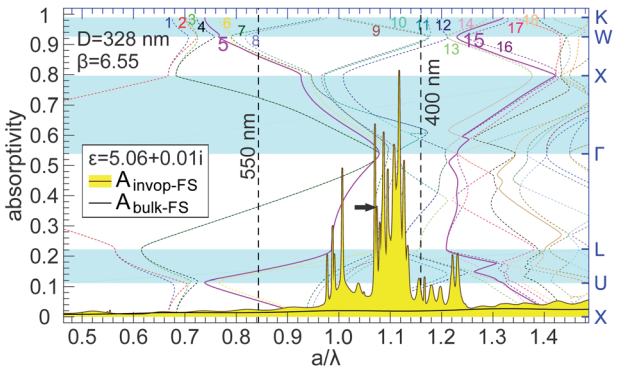

Fig. 4 Absorptivity spectra of a 6-layer invop-FS architecture with $D = 328$ nm and the planar bulk-FS of equivalent bulk thickness, for the dispersionless dielectric Model I.01. The background dashed curves depict the invop photonic bands, with the 5th and 15th bands highlighted. The vertical black dashed lines demark the [400, 550] nm wavelength range within which β is calculated. The thick black arrow indicates an optical resonance at $a/\lambda = 1.074$, for which the energy and Poynting vector distributions are plotted in Fig. 14.

3.2 Slow light modes for strong absorption enhancement

To optimize the light absorption enhancement, we scan the invop voids center-to-center distance D in Fig. 3 and look for the average absorptivity and its enhancement factor β in the wavelength region of $\lambda \in [400, 550]$ nm using the dielectric Model I.01. The influence of varying ε'' on light trapping is discussed in App. D. Fig. 3 reveals that β of the invop-FS architecture is dramatically increased when D is around 320 nm. In this case, both the red- and the blue-edge modes are displaced to frequencies well below the absorption spectrum of TiO_2. At $D = 328$ nm, β reaches 6.55 (corresponding to $A_{avg} = 12.0\%$), which is 4.5 times of that of the red-edge modes that are operative when $D = 159$ nm (see also Table 1 for summary).

The absorption spectrum for $D = 328$ nm is superimposed with the invop PC band diagram in Fig. 4 to identify the photonic modes responsible for the dramatic absorption enhancement. A high density of strongly absorptive resonant photonic modes between the 5th and 15th bands are excited by light at normal incidence. The number and density of these higher order modes far exceed the red- and blue-edge modes. This remains true for invop-FS with more opal layers [see Fig. 12 and 17(b)]. These photonic modes are especially effective for light trapping due to their large transverse Poynting vectors (see Fig. 14 and the discussion in App. C). For example, at $a/\lambda = 1.074$, the absorptivity reaches 36.4% for $\varepsilon'' = 0.01$.

Light trapping is further boosted by replacing the FS substrate with a highly reflective substrate, as shown in Fig. 3. A mirror substrate enhances the average absorptivity by a factor of $\sim$2 by reducing the transmission loss.[28,29] It also increases the optimized value of D by $\sim$30 nm due to the modification of the photonic modes: in the invop-FS architecture $\beta = 6.55$ at $D = 328$ nm for $\lambda \in [400, 550]$ nm for dielectric Model I.01, while in the invop-MR architecture $\beta = 11.53$ at $D = 352$ nm. Overall the inverse opal center-to-center distance $D \sim$ 320–380 nm represents the optimized structure for sub-gap optical absorption for both invop-FS and invop-MR. A mirror substrate may also

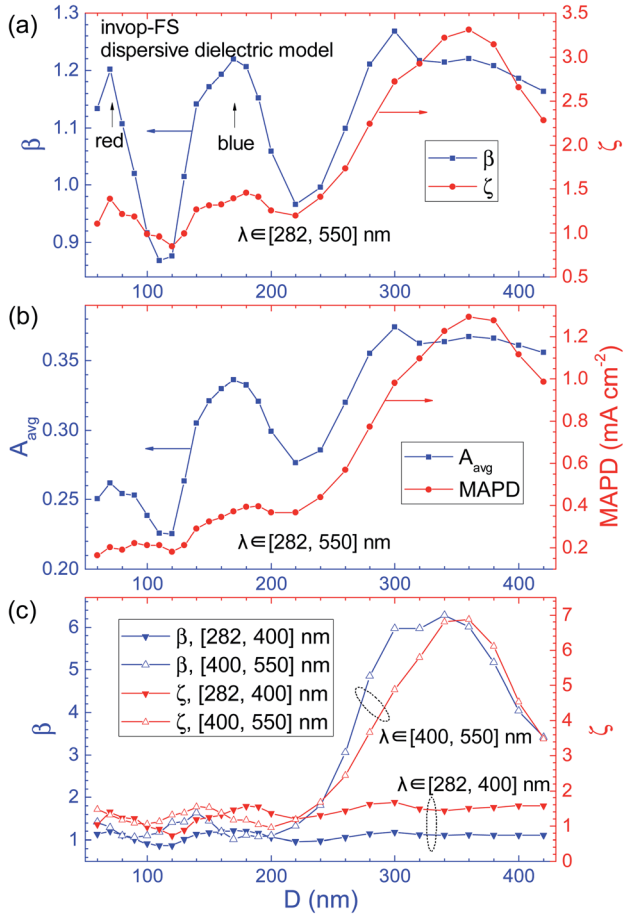

Fig. 5 The average absorptivity A_{avg} and maximum achievable photocurrent density (MAPD) as well as their enhancement factors β and ζ for a 6-layer invop-FS architecture as functions of D using the dispersive dielectric Model II.01 in the wavelength regions of (a and b) $\lambda \in$ [282, 550] nm and (c) $\lambda \in$ [282, 400] nm and [400, 550] nm.

facilitate the electron–hole separation by forming a metal–semiconductor junction, reducing the photogenerated charge carrier recombination.[30]

Beyond better light trapping ability, there are further advantages of using higher order photonic modes. The narrow bandwidth of the red- and blue-edge modes makes them more difficult to align with the TiO_2 electronic band edge (the most efficacious alignment of these two edges) due to the unpredictable template shrinkage and unruly TiO_2 filling fraction during infiltration. Photonic bands 5 to 15 avoid this issue because they cover a wide spectral region. This relaxes the requirement of the stringent control on the PC lattice constant (Fig. 3, 5 and 8) and incident angle (Fig. 18). It also enables carrier photogeneration deeper into the high intensity visible solar spectrum without excess doping or other modifications of TiO_2 with concomitant recombination centers. High absorptivity is achieved with higher order photonic bands despite weak, intrinsic, visible-light absorption in TiO_2 in a way that is not possible with the red- and blue-edge modes. This is discussed in Sec. 4.

4 Optimization of photocatalytic efficiency with structure

The dispersionless dielectric Model I is valuable for identifying invop photonic modes that are optimum for light trapping in the spectral region of weak absorption in TiO_2. However, TiO_2 has large material dispersion at and above the electronic band edge and becomes strongly absorbing of the scarce sunlight for $\lambda < 400$ nm. The nonuniform solar illumination spectrum and the strong frequency dependent absorptivity of TiO_2 necessitates careful alignment of the higher-order slow-light modes with respect to the anatase electronic bands and the solar spectrum to yield the best solar-driven photocatalytic efficiency. In this section we focus on the MAPD enhancement factor ζ over the full UV to visible region of $\lambda \in$ [282, 550] nm for different sphere sizes of the invop PC using the dispersive dielectric Model II introduced in Sec. 3 and App. A.1.

In Fig. 5(a), the absorptivity enhancement factor β (lowered by including the strong above-electronic-gap absorption) exhibits three comparable maxima at the opal center-to-center distance $D = 70$ nm, 170 nm, and 300 nm. These peaks correspond to the alignments of the red-edge mode and the blue-edge mode to the nearby of the electronic band edge and the higher-order slow-light modes to the $\lambda \in$ [400, 550] nm wavelength region, respectively (see Fig. 6 and 7).

4.1 The red-edge and blue-edge modes revisited

We now compare the red- and blue-edge slow photons in Fig. 5 when the material dispersion is included (Model II). Here we no longer isolate the red- and blue-edge modes and align them to a particular frequency. Contributions over the entire UV to visible range are included from all the photonic modes. The labels of "red-edge" and "blue-edge" simply indicate the modes that provide dominant contribution.

In contrast to Sec. 3.1, the blue-edge peak now demonstrates stronger light harvesting ($\beta = 1.22$ at $D = 170$ nm) than the red-edge peak ($\beta = 1.20$ at $D = 70$ nm). This behavior persists in MAPD when including the solar spectrum: $\zeta = 1.39$ at $D = 170$ nm and $\zeta = 1.45$ at $D = 180$ nm for the blue-edge peak, compared with $\zeta = 1.38$ at $D = 70$ nm for the red-edge peak. The actual values of A_{avg} and the MAPD are plotted in Fig. 5(b). The difference between the blue- and red-edge peaks appears greater now because the former (utilizing larger opal spheres) contains a larger volume of TiO_2 in the same six layers.

The absorptivity and reflectivity spectra of the invop-FS architectures, including the red- and blue-edge contributions are given in Fig. 6. For $D = 70$ nm, the fundamental stop gap resides inside the anatase conduction band, so no strong reflection peak is observed in Fig. 6(a). The red-edge is aligned just above the electronic band edge, enabling some light-trapping enhancement near the conduction band edge. For $D = 110$ nm, the fundamental stop gap moves to the anatase conduction band edge, blocking light around this frequency from entering the invop PC. This reduces the absorptivity and MAPD, which manifests in Fig. 5 as significant dips around $D = 110$ nm. For $D = 130$ nm, the fundamental stop gap moves

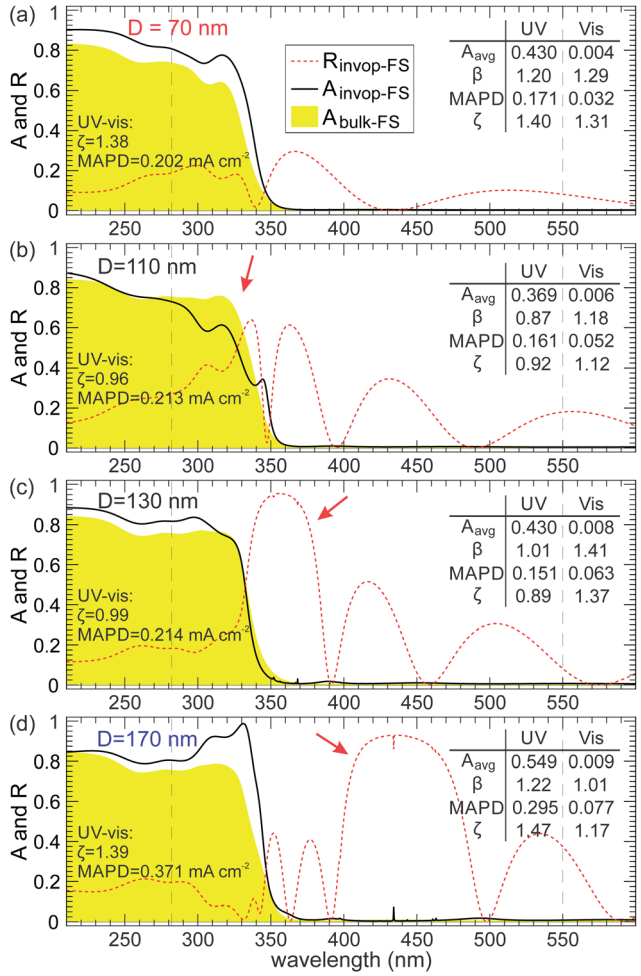

Fig. 6 Absorptivity and reflectivity (R) spectra of a 6-layer invop-FS and bulk-FS architectures for (a) $D = 70$ nm (b) $D = 110$ nm, (c) $D = 130$ nm and (d) $D = 170$ nm using the dispersive dielectric Model II.01. The vertical black dashed lines mark the wavelength of 282 nm and 550 nm. The red arrows indicate the fundamental reflection peaks. The "UV", "Vis" and "UV-vis" in the table insets stand for the regions of $\lambda \in [282, 400]$ nm, $\lambda \in [400, 550]$ nm, and $\lambda \in [282, 550]$ nm, respectively, and the unit of MAPD is mA cm^{-2}.

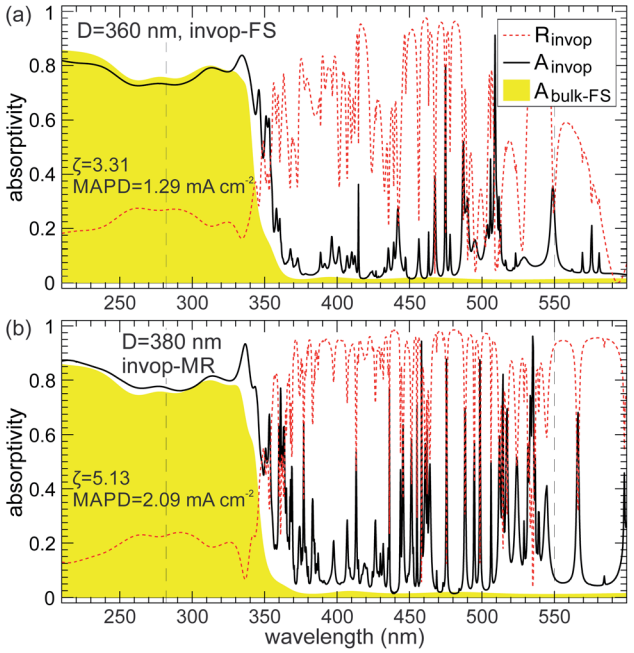

Fig. 7 Absorptivity and reflectivity spectra of a 6-layer (a) invop-FS for $D = 360$ nm and $d = 380.1$ nm, (b) invop-MR for $D = 380$ nm and $d = 401.2$ nm, and bulk-FS architectures using the dispersive dielectric Model II.01. The vertical black dashed lines demark the spectral region of $\lambda \in [282, 550]$ nm over which MAPD and ζ are calculated.

slightly below the anatase conduction band edge and the blocking effect is less severe. Light harvesting improves toward $D = 170$ nm, at which point the fundamental stop gap, including its immediate short-wavelength edges, falls completely within the electronic band gap and the further blue-edge now traps light around the electronic band edge. Although the blue-edge has a slightly lower light trapping ability within the TiO_2 backbone than the red-edge (as discussed in Sec. 3.1), it provides higher β and ζ, in agreement with previous work.[18] However, there is no significant contribution to carrier photogeneration from sub-gap electronic transitions.

4.2 Light harvesting using higher order slow-light modes in the visible range

The third and highest peak in Fig. 5(a) occurs when the higher order slow-light modes (between the 5th and 15th bands) are placed into the visible range $\lambda \in [400, 550]$ nm. This is depicted in Fig. 7(a). Although β is comparable to that of the red- and blue-edge peaks, the MAPD enhancement factor $\zeta = 3.31$ at $D = 360$ nm is 2.28 times that of the blue-edge peak with $\zeta = 1.45$ at $D = 180$ nm. This dramatic improvement comes from the remarkable visible light harvesting by higher order slow-light modes.

In Fig. 5(c) we break the spectrum into UV ($\lambda \in [282, 400]$ nm) and visible ($\lambda \in [400, 550]$ nm) parts for comparison. In the UV region, light harvesting remains weak irrespective of photonic modes because the intrinsic TiO_2 absorptivity in this region is

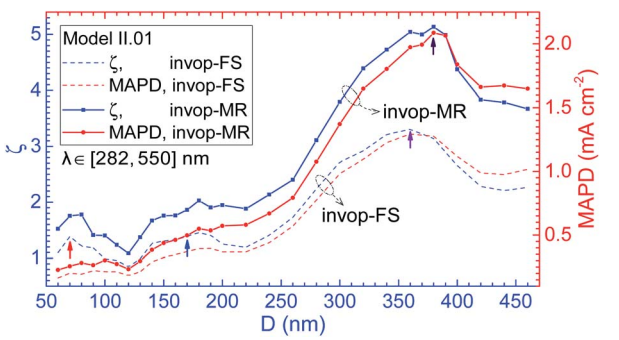

Fig. 8 The MAPD (red lines) and its enhancement factors ζ (blue lines) for 6-layer invop-FS (dashed lines) and invop-MR (solid lines) architectures as functions of D using the dispersive dielectric Model II.01 in the wavelength regions $\lambda \in [282, 550]$ nm. The red, blue, purple, and dark purple arrows mark the cases shown in Fig. 6(a), (d) and 7(a), (b), respectively.

already high and solar illumination is weak. The lack of contrast in β and ζ in the UV spectral range reveals the inefficiency of aligning the PC slow-light modes near to the TiO_2 electronic band edge. But in the visible light region, the higher-order slow-light modes provide $\zeta = 6.87$ times MAPD enhancement at $D =$ 360 nm. This is because the number of solar photons for $\lambda \in$ [400, 550] nm is six times of that in the UV range, amplifying the effect of light-trapping in the visible region. Overall, $D \approx$ 360 nm (opal sphere diameter $d \approx 380.1$ nm) is the optimum invop-FS architecture PC for enhanced photocatalytic efficiency.

The fused silica substrate was used above to make comparison with past experiments with invops placed on transparent supports. However, more efficient light harvesting is achieved when the same invop PC is placed on a highly reflective substrate as discussed in Sec. 3.2. This is illustrated in Fig. 8 and 7(b). Comparing Fig. 7(a) and (b), the MAPD enhancement factor is increased from 3.31 for the invop-FS architecture to 5.13 for the invop-MR architecture (with $D = 380$ nm, $d = 401.2$ nm). The results are summarized in Table 1.

So far we have considered invop PCs with only 6 opal layers. Experimentally, many more opal layers can be prepared. This adds more anatase to the photocatalyst and improves the MAPD as shown in Fig. 9. Comparing with Fig. 8, the effectiveness of the mirror substrate is very apparent. For the same $D = 360$ nm, the 6-layer (1.850 μm thick) invop-MR architecture yields higher MAPD than the 20-layer (5.965 μm thick) invop-FS architecture. At $D = 380$ nm, the 8.158 μm-thick 26-layer invop-MR architecture demonstrates MAPD of 3.23 mA cm^{-2}.

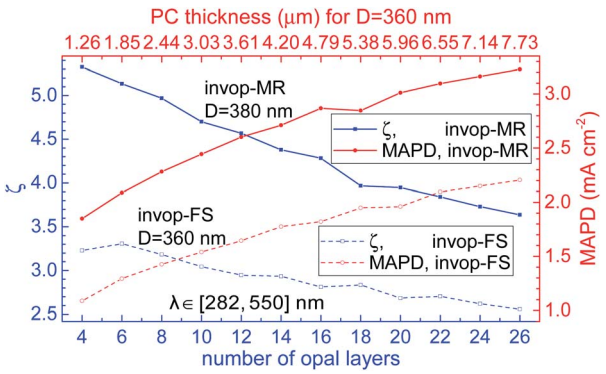

Fig. 9 The MAPD and its enhancement factor ζ for architectures of invop-FS with $D = 360$ nm (dashed lines) and invop-MR with $D =$ 380 nm (solid lines) with increasing number of opal layers in the wavelength region of $\lambda \in$ [282, 550] nm under the dispersive dielectric Model II.01.

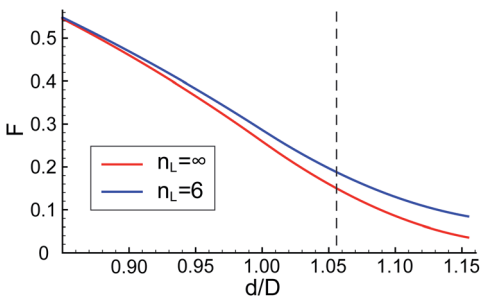

Fig. 10 The filling fractions of invop PC in our model as a function of d/D for $n_L \to \infty$ and $n_L = 6$, respectively. The dashed line marks the case of $d/D = 1.0558$ for which $F = 15\%$ for $n_L \to \infty$.

5 Conclusion

In summary, we have identified a substantially improved architecture for photocatalytic response in anatase TiO_2 inverse opal photonic crystals. This involves the use of opal spheres with diameter $d \sim 380$ nm, in constrast to widely studied small-sphere inverse opals. Our new mechanism of light trapping involves higher order slow-light modes with substantial transverse energy flow perpendicular to normally incident sunlight. These modes occur at higher frequency than traditional "red-edge" and "blue-edge" slow light. The modes reside between bands 5 and 15 of the photonic crystal and their optimized alignment is slightly below the TiO_2 electronic band edge. This greatly enhances visible light absorption in the 400–550 nm range of lightly doped TiO_2.

The light harvesting abilities of the red-edge and blue-edge slow-light modes are comparable to each other, but considerably weaker than the higher order slow-light modes we have identified. In a dispersionless dielectric medium the red-edge is slightly superior to the blue-edge for light harvesting. However, near the electronic band edge of anatase TiO_2 the blue-edge is slightly superior to the red-edge. Nevertheless, the differences are marginal and experimentally indistinguishable. Neither edge of the fundamental stop gap is ideal for photocatalysis and the light harvesting enhancement is weak around the electronic band edge irrespective of the slow-light modes. Instead, we suggest that future effort focus on the improvement of the sample quality in order to utilize higher order bands of the inverse opal in the visible region, with voids' center-to-center distance $D \sim 360$ nm, created from opal spheres of diameter $d \sim 380$ nm.

A wide range of the sphere sizes of opal templates have been tested in past experiments.[20] The highest reported photocatalysis enhancements so far are from slow-light modes surrounding the fundamental stop gap. This is likely due to limited bandwidth of irradiation, sparse sampling of the opal sphere size, strong sensitization and modification of TiO_2, or degradation of the higher photonic slow-light modes because of low quality PC samples (see discussions in App. E).

With high-quality lightly-doped TiO_2 inverse opals, operating in the optimum regime, light trapping capability is predicted to be ~5 times better than the red- and blue-edge modes. It is our hope that these considerations will lead to fuller exploitation of photonic crystal light trapping for efficient photocatalysis.

Appendix A Models of anatase TiO_2 and the inverse opal PC

A.1 Dielectric models

The photocatalyst is assumed to be lightly doped anatase TiO_2, with shallow defect states below the conduction band

minimum and above the valance band maximum. Both the Shockley–Read–Hall bulk recombination rate and the surface recombination rate are proportional to the density of defect states. A light doping of TiO_2 ensures weak carrier recombination while enables strong photogeneration implemented by photonic slow-light modes on band tail states for visible light harvesting. Precise optical properties of anatase, including the absorption band gap, vary with preparation details. We consider two categories of optical models of lightly doped anatase to encompass light harvesting in various doping and defect scenarios. These categories consist of a dispersionless Model I and a dispersive Model II.

The dispersionless Model I of anatase focuses on sub-gap, band tail electronic transitions and the dielectric constant $\varepsilon = \varepsilon' + i\varepsilon''$ is independent on the frequency. This is convenient for identification of optimal photonic modes for light trapping, and enables generalization to structural and spectral rescaling. We introduce a scaling factor $0.87 \lesssim s \lesssim 1.3$ to accommodate small variations in the spectral region of interest. The bounds on the scaling factor, s, ensure that spectral region considered stays within the region of sub-gap electronic transitions. The conclusions in Sec. 3 remain valid in the wavelength range of $\lambda \in [400s, 550s]$ nm when the invop voids center-to-center distance is scaled from D nm to Ds nm. Since different anatase samples may exhibit different sub-gap absorptivities, we consider a range of values for the imaginary part, $0.001 \leq \varepsilon'' \leq 0.1$. The nomenclature, Model I.x refers to the case when $\varepsilon'' = 0.x$.

In the dispersive Model II of anatase, we incorporate the realistic material dispersion around and above the electronic band gap by adopting an experimentally measured result[27] on the single crystal anatase. As the TiO_2 invop samples used for photocatalysis are rarely in their single crystal forms, the dielectric function of a polycrystal anatase is taken as a coarse-grained average of the dielectric functions over the three orthogonal polarizations (along and perpendicular to the optical axis) of light in a single crystal. The real part of the dielectric function in ref. 27 is given in the UV to visible spectral range, while the imaginary part is unresolved in the sub-gap region in this high quality crystal. For continuity with the dispersionless Model I, a small constant imaginary part of the dielectric function is appended to the experimental data of ref. 27 below the electronic band gap ~3.5 eV to mimic the light doping of the sample. This hybrid dielectric model allows the optimized alignment of the invop photonic modes with respect to the electronic bands of TiO_2. The nomenclature, Model II.x, refers to the case when $\varepsilon'' = 0.x$ in the sub-gap region.

Since photocatalytic environmental remediation often involves the decomposition of aqueous pollutants, we always assume the PC backbone is immersed in water and its solutes, with the solution refractive index $n_{H_2O} = 1.33$. The refractive index of the FS substrate is taken to be 1.46.

A.2 Structural model

The invop PC is commonly fabricated in a bottom-up approach by infiltrating a colloidal crystal template, made of self-assembling monodisperse silica or polymer spheres of diameter 100 nm $\lesssim d \lesssim$ 1000 nm.[31,32] Methods include sol–gel synthesis,[31,33–35] chemical vapor deposition,[36,37] atomic layer deposition (ALD)[38,39] and electrodeposition.[40] We model the resulting structure as anatase TiO_2 completely backfilling (*i.e.*, no air pockets in interstitial sites of spheres) a face-centered cubic opal crystal, composed of void (water) spheres of diameter d and nearest neighbor center-to-center distance D,[18] as shown in Fig. 1(a). The height of the complete infiltration is the same as the opal crystal. The effect of incomplete infiltration on the photonic bands was discussed in ref. 41. The PC has a finite height along the natural growth direction [111], and for our modeling is assumed infinite along the plane perpendicular to [111]. The sintering effect of the opal template, which has been modeled by adding tubelike bonds between adjacent spheres,[41] is neglected.

Consider a finite size sample consisting of n_L stacked layers and periodically repeating unit cells with transverse sizes $s_x = D$, $s_y = \sqrt{3}D$ (such as that shown in Fig. 13 and 14). The vertical size of the finite PC thickness is given by $d_{PC} = (n_L - 1)d_{pch} + d$, where $d_{pch} = (\sqrt{6}/3)D$ is the layer pitch. The volume of a unit cell column is $V_{cell} = s_x s_y d_{PC}$. Each opal sphere in the top and bottom layers has 9 nearest neighbors. All interior opal spheres have 12 nearest neighbors. For $D \leq d \leq (2/\sqrt{3})D$, each truncated opal sphere in the top and bottom layers has a volume of a whole sphere minus 9 missing caps. All other truncated opal spheres have the volume of a whole sphere minus 12 missing caps. Adding all these truncated opal spheres together, the total opal volume per unit cell column, for $n_L \geq 2$, is given by:

$$\pi\left[-\left(n_L - \frac{3}{5}\right)\frac{5}{3}d^3 + \left(n_L - \frac{1}{2}\right)3d^2D - \left(n_L - \frac{1}{2}\right)D^3\right].$$

The filling fraction F is equal to one minus the volume ratio between the opal voids and the overall cell. For an inverse opal with voids partially overlapping one another ($D \leq d \leq (2/\sqrt{3})D$), this becomes:

$$F = 1 - \frac{\pi}{3\sqrt{2}}\left(-5\eta^3 + 9\eta^2 - 3\right)\frac{n_L}{n_L + \sqrt{3/2}\eta - 1} - \frac{\pi}{2\sqrt{2}}\frac{2\eta^3 - 3\eta^2 + 1}{n_L + \sqrt{3/2}\eta - 1}, \quad (5)$$

where $\eta = d/D \in [1, 2/\sqrt{3}]$. The filling fraction for a finite height invop is clearly n_L-dependent (see Fig. 10). This is important for the correct mass-normalization of A_{avg} and MAPD to obtain their enhancement factors β and ζ, respectively.

The surface area per unit volume of the invop structure decreases inversely with increasing D. As the photogeneration occurs in the bulk while the carrier recombination primarily takes place on the surface of inverse opals, the use of larger spheres provides a major improvement in photogeneration through higher-order, slow-light modes while suppressing the dominant surface recombination. On the other hand, for a given number of opal spheres, the surface area of the invop increases roughly as D^2. In such a case there is synergy between light trapping and surface redox reactions for our proposed increase in opal size.

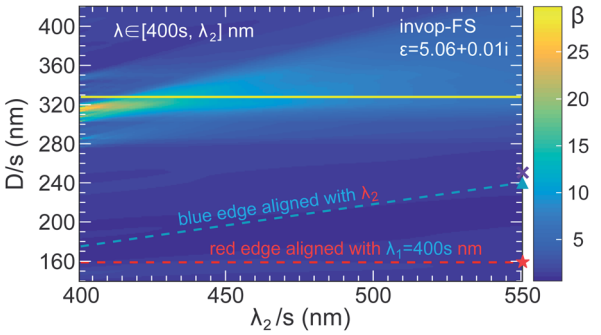

Fig. 11 The color map of β in the range of $\lambda \in [400s, \lambda_2]$ nm for the 6-layer invop-FS architecture using the dispersionless dielectric Model I.01. The red and blue dashed lines define the loci of points at which red edge coincides with the high frequency spectral limit $\lambda_1 = 400s$ nm and the blue edge coincides with the low frequency spectral limit λ_2, respectively. The solid yellow line identifies $D = 328s$ nm (opal sphere diameter $d = 346.3s$ nm). The markers of red star and light-blue triangle correspond to Fig. 2(a) and (b), respectively. The thin purple cross represents the case shown in Fig. 2(b) with $\lambda_2 = 550$ nm aligned to the thin purple cross therein. A large absorptivity enhancement $\beta \sim 20$ is seen for $D \sim 320s$ nm due to light-trapping in higher order slow-light modes well above the blue edge.

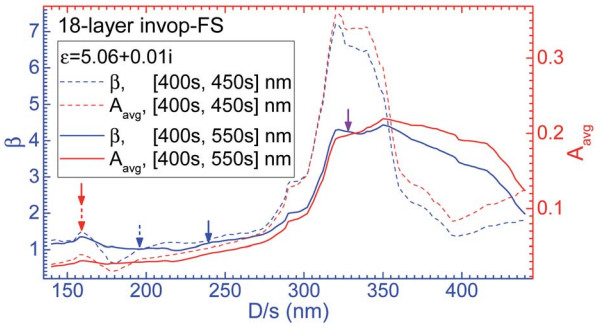

Fig. 12 Average absorptivity A_{avg} (red lines) and its enhancement β (blue lines) of an 18-layer invop PC on a FS substrate as functions of D in the wavelength region of $\lambda \in [400s, 450s]$ nm (dashed lines) and $\lambda \in [400s, 550s]$ nm (solid lines) using the dispersionless dielectric Model I.01. The red dashed and solid arrows indicate the voids' center-to-center distance D that place the short-wavelength limit of the spectral ranges of interest at the red edge of the fundamental stop gap. The blue dashed and solid arrows indicate the values of D that place the long-wavelength limit of the spectral regions of interest at the blue edge of the fundamental stop gap. The purple arrow marks the case that higher-order slow-light modes fall into the $\lambda \in [400s, 550s]$ nm range.

Appendix B Rescaling of the sub-gap spectral range for 6- and 18-layer invop-FS architecture

Different experiments for photocatalysis focus on different wavelength ranges. Our comparison in Sec. 3.1 of the red- and blue-edge slow-light modes using Model I is based on the spectral region of $\lambda \in [400, 550]$ nm. To generalize the spectral range, we scan λ_2 and take advantage of the scaling property of Maxwell's equation for the frequency-independent dielectric function of Model I. The scaling factor $0.87 \lesssim s \lesssim 1.3$ is restricted in range to avoid erroneous extrapolation into a highly dispersive region of TiO_2. The color map of β in a spectral range of $\lambda \in [400s, \lambda_2]$ using the dispersionless dielectric Model I.01 is given in Fig. 11.

Along the red-dashed line, $\lambda_1 = 400s$ nm is aligned with the red edge of the fundamental photonic stop gap in the band diagram as λ_2 is varied. Along the blue dashed line λ_2 is fixed to the blue edge and then varied. For example, in the case of $s = 0.95$, the vertical cut at $\lambda_2/s = 550$ nm in Fig. 11 renders the average absorptivity enhancement β in the spectral range of $\lambda_1 = 400s$ nm to $\lambda_2 = 550s$ nm, namely, $\lambda \in [380, 522.5]$ nm, as a function of D. In this case, the red-edge of the fundamental photonic stop gap in the band diagram is placed at $\lambda_1 = 380$ nm when $D = 159s = 151$ nm. In this case, the blue-edge of the fundamental photonic stop gap is placed at $\lambda_2 = 522.5$ nm when $D = 240s = 228$ nm.

In general the value of β along the red cut is higher than that along the blue cut. This is further verified in an 18-layer invop-FS architecture using the dispersionless dielectric Model I.01 in both $\lambda \in [400s, 450s]$ nm and $\lambda \in [400s, 550s]$ nm regions (see Fig. 12).

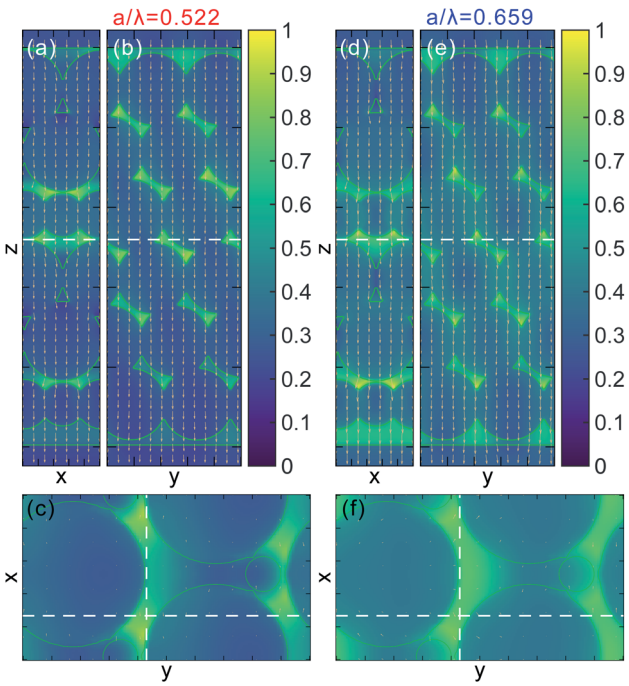

Fig. 13 Distributions of electromagnetic energies (color map) and Poynting vectors (pale-gold arrows) at the "red-edge" (a–c) $a/\lambda = 0.522$ and the "blue-edge" (d–f) $a/\lambda = 0.659$ of the 6-layer invop PC placed on a FS substrate. The contour plots outline the real part of the dielectric constant. (a and b) The longitudinal cuts corresponding to the white dashed lines in (c). (d and e) The longitudinal cuts corresponding to the white dashed lines in (f). (c and f) The transverse cuts at the position indicated by the white dashed lines in (a, b) and (d, e), respectively.

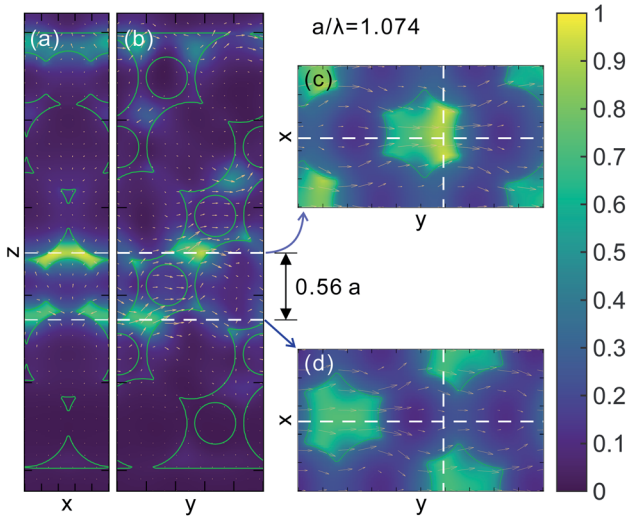

Fig. 14 Distributions of electromagnetic energies (color map) and Poynting vectors (pale-gold arrows) for the higher order slow-light mode with $a/\lambda = 1.074$ of the 6-layer invop-FS architecture. (a and b) The longitudinal cuts at fixed values of y and x directions, respectively, indicated by the white dashed lines in (c) and (d). (c and d) The transverse cuts at fixed values of z, separated by $0.56a$, marked by the white dashed lines in (a) and (b).

Appendix C Electromagnetic energy and poynting vector distributions of various slow-light modes

The spatial field profiles of red-edge and blue-edge slow-light modes are illustrated in Fig. 13 at the frequencies of $a/\lambda = 0.522$ and 0.659, respectively. These are compared in Fig. 14 with a higher order slow-light mode at $a/\lambda = 1.074$.

In Fig. 13 we investigate the energy and Poynting vector patterns at the red and blue edges of the fundamental photonic stop gap. As discussed in previous literature,[8] the electromagnetic energy on the red side of the stop gap resides primarily in the TiO_2 backbone, while on the blue side it concentrates more in water. This causes slightly higher absorptivity at the red-edge than blue-edge. The difference is only slight since substantial energy overlaps the absorptive backbone (anatase) in either case.[18] However, energy distributions alone do not determine absorptivity. Another critical factor is the flow pattern and dwell time of light in the structure. In a thin ($\sim$10 layer) invop sample, propagation of light along the layer planes implies much longer dwell time and higher absorption than propagation normal to the layer planes. This requires consideration of the electromagnetic Poynting vector fields within the sample for different slow-light modes.

Fig. 13 reveals that for both red- and blue-edge modes the energy flux is primarily along the [111] direction, which has a small finite thickness. Light traveling along this direction quickly escapes. On the other hand, along transverse directions the PC is practically infinite and light cannot escape. Light diffracted and scattered into transverse directions has long dwell time and is more likely to be eventually absorbed. To evaluate the energy flux, we introduce the average fraction of the transverse Poynting vector as

$$\sigma = \frac{1}{V}\int \frac{|S_{xy}|}{|S|} \mathrm{d}V, \tag{6}$$

where V is the volume, S is the Poynting vector and S_{xy} is its transverse component. σ measures the volume-average tendency for energy flow in the transverse directions. At the red-edge ($a/\lambda = 0.522$) $\sigma = 0.057$ and at the blue-edge ($a/\lambda = 0.659$) $\sigma = 0.068$. This explains the relatively weak light trapping of slow light around the fundamental photonic stop gap of a thin film of invop PC.

Much stronger light trapping due to transverse energy flow is achieved using higher order photonic modes. As an example, the electromagnetic energy and Poynting vector distributions for a slow-light mode at the frequency of $a/\lambda = 1.074$ are plotted in Fig. 14. Compared to the red-edge mode, the energy is focused more strongly inside the anatase than in the voids. More importantly, the Poynting vector has a significant component in the transverse direction, especially in the high-energy density regions. For this higher order slow-light mode, $\sigma = 0.86$, 15 times of that of the red-edge mode. This transverse flow of energy implies a relatively long dwell time, leading to a large absorptivity enhancement. These transverse slow-light modes are much more effective in light harvesting than the red- and blue-edge slow-light modes surrounding the fundamental stop gap.

Appendix D Robustness of light trapping with higher order slow-light modes

Matching of the dwell time of light in an optical cavity with the material absorption time is important for strong absorption.[28,29] The absorption time is determined by the dielectric constant. Accordingly, the PC-based absorptivity enhancement varies with the dielectric function of anatase. TiO_2 can be prepared with a wide range of material absorptivities below the electronic conduction band by doping and sensitization. We consider a range of values, $\varepsilon'' = 0.001$, 0.01, 0.05, and 0.1 in the dispersionless dielectric Model I, to evaluate the robustness of the light harvesting enhancement.

Fig. 15 reveals that higher ε'' leads to larger A_{avg}. In constrast, the enhancement factor β drops as ε'' increases. This is clearly seen for higher-order slow-light modes (the $D \gtrsim 300s$ nm region). This is because the fraction of absorbed light in an already highly absorptive medium cannot be improved greatly (absorption saturation) by light trapping effects. Nevertheless, $D \sim 320s$ nm appears optimal for absorption enhancement in the $\lambda \in [400s, 550s]$ nm region for broad range of choices of ε'' in the dispersionless dielectric Model I.

Due to absorption saturation, it is not optimal to align higher-order slow-light modes to the TiO_2 electronic band edge. This manifests in Fig. 5(c) in the $\lambda \in [282, 400]$ nm region as the lack of enhancement contrast as a function of D. However, in the sub-gap region, where the solar irradiation is intense, the higher order

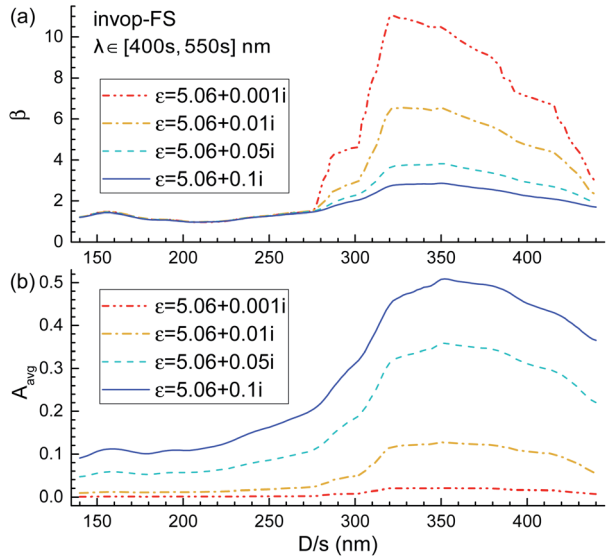

Fig. 15 (a) Absorptivity enhancement β and (b) average absorptivity A_{avg} of a 6-layer invop PC on a FS substrate as functions of D in the wavelength region of $\lambda \in [400s, 550s]$ nm. The dispersionless dielectric Model I is used with different imaginary parts $\varepsilon'' = 0.001$, 0.01, 0.05, and 0.1.

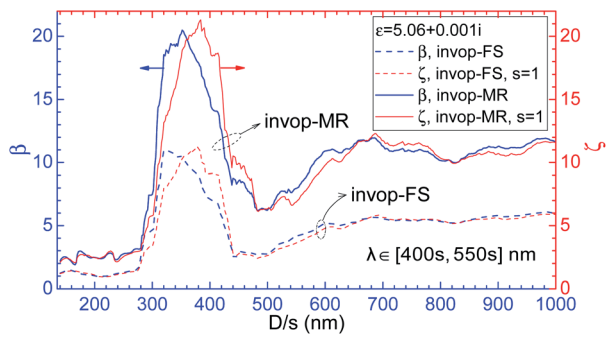

Fig. 16 The absorptivity enhancement β and MAPD enhancement ζ of a 6-layer invop PC on FS and MR substrates as functions of D in the wavelength region of $\lambda \in [400s, 550s]$ nm ($s = 1$ for ζ) for the dispersionless dielectric Model I.001 with $\varepsilon = 5.06 + 0.001i$.

slow-light modes are of remarkable utility in light harvesting. This is shown in Fig. 16 where we plot the absorptivity enhancement β and MAPD enhancement ζ as functions of D for both invop-FS and invop-MR architectures using the Model I.001. When $\varepsilon = 5.06 + 0.001i$, $\beta = 11.05$ at $D = 322s$ nm for invop-FS architecture, which is 7.6 times that of the red-edge.

Appendix E The "red", "blue", and "bluer" in experiments

In experiments, positioning of the photonic bands usually relies on the measurement of the reflection or transmission spectrum. As the bands numbers are not direct observables, positioning has relied on a crude estimation of the diffraction wavelength by the modified Bragg formula,[10,11,14,42] $\lambda = (2d_L/m)(n_{eff}^2 - \sin^2\theta_{in})^{1/2}$, where d_L is the spacing between the

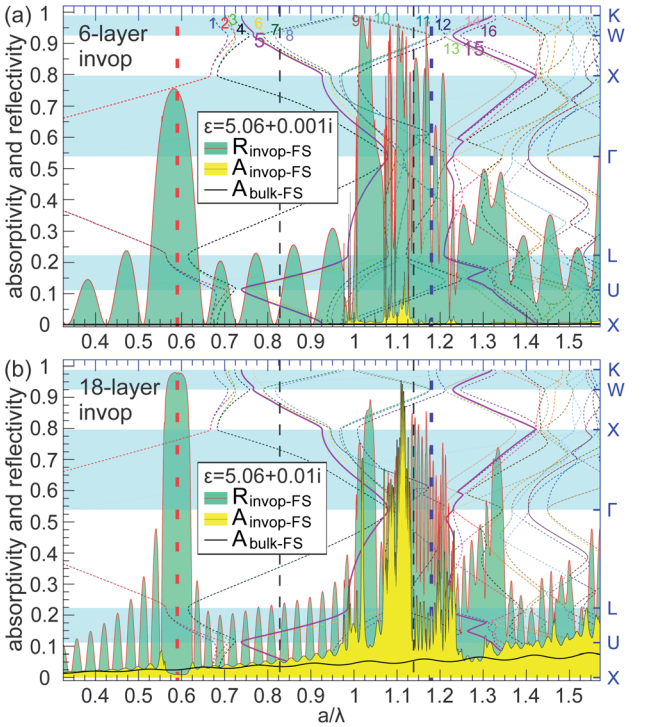

Fig. 17 The absorptivity and reflectivity spectra of a (a) 6-layer and (b) 18-layer invop PC on FS substrate for dispersionless dielectric Models (a) I.001 and (b) I.01, respectively. The background dashed curves depict the inverse opal PC band diagram, with the 5th and 15th bands highlighted. The vertical thin black dashed lines demark the wavelengths $\lambda \in [400, 550]$ nm for the case of $D = 322$ nm. The vertical thick red and blue short dashed lines mark the first ($a/\lambda = 0.59$) and purported second ($a/\lambda = 1.18$) order diffraction peaks, respectively, based on the modified Bragg formula with $d_L = (\sqrt{6}/3)D$, $\theta_{in} = 0$, $n_{TiO_2} = 2.25$, $n_{H_2O} = 1.33$, and $F = 0.15$.

structural layers, m is the diffraction order, θ_{in} is the incident angle, and $n_{eff} = n_{TiO_2}F + n_{H_2O}(1 - F)$ is a simplistic effective refractive index. In Fig. 17(a) we plot the reflection and absorption spectra of a 6-layer invop PC placed on a FS substrate using the dispersionless dielectric Model I. The observed reflection peak at $a/\lambda = 0.584$ due to the fundamental stop gap along the Γ–L direction agrees with the band diagram of an infinite-size invop PC. A value of $a/\lambda = 0.59$ for this peak is obtained from the modified Bragg formula. However, the "second order Bragg reflection" peak along Γ–L is predicted at $a/\lambda = 1.18$ by the modified Bragg formula. This disagrees with the major reflection peaks obtained from exact FDTD simulation. The modified Bragg formula is inaccurate in a strongly scattering system except for the lowest order peak.

For $a/\lambda < 1.18$, a large number of photonic modes are accessible by normally incident light (see Fig. 17). These accessible modes are intermingled with densely packed reflection spikes, which together appear roughly as a high reflection region. The most efficacious slow-light modes, identified in this work, reside inside the low-frequency side of the purported second order Bragg reflection. These strong absorptive higher-order, slow-light modes, although interspersed among reflection spikes, nevertheless provide a significant overall increase in light harvesting.

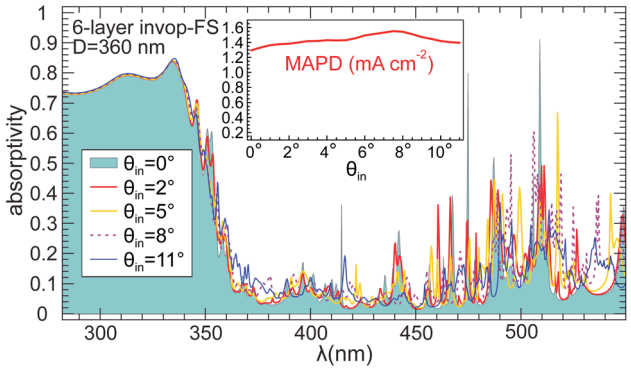

Fig. 18 The absorptivity spectra of the 6-layer invop-FS architecture with $D = 360$ nm using the dispersive dielectric Model II.01 under normal ($\theta_{in} = 0°$) and oblique ($\theta_{in} = 2°$, 5°, 8°, and 11°) incidences, where θ_{in} is the incident angle. The inset plots the MAPD as a function of θ_{in} in the $\lambda \in [282, 550]$ nm spectral range.

High sample quality is essential to resolve the sharp and narrow reflectivity peaks, between bands 5 and 15, depicted in Fig. 17. This high quality of structural order is not evident in previous experiments exploring higher order bands. The purported second order Bragg reflection is not observed in most experiments. There are a few works reporting the observation of second order Bragg reflection peaks in invop PCs made by sol–gel infiltration of (modified) TiO_2 (ref. 42) and ZnO,[14] and direct embedding of polystyrene opals in TiO_2 nanoparticle matrix.[43] However, the individual reflection peaks shown in Fig. 17 around the frequencies of $a/\lambda \sim 1.1$ were not resolved. For ZnO invop PC, it was suggested that the red edge of the purported second order stop gap provides better photocatalytic efficiency than the blue edge.[14] Other works allude to the role of higher photonic bands in photocatalysis[8,44,45] without detailed evidence.

A more promising approach is the ALD method for TiO_2 infiltration of self-assembled opal templates. This has demonstrated finer resolved higher order reflection spectra.[38,39,46] A high-resolution infiltration method combined with very high-quality opal templates[36] and using ~380 nm diameter opal spheres, may enable exploitation of the higher-order slow-light modes for enhanced photocatalytic efficiency.

The light absorptivity due to these optimized higher-order slow-light modes are much more robust against the variation of incident angles θ_{in} comparing with the red and blue slow-light modes. Fig. 18 shows that photonic resonances shift and changes with θ_{in}, and light trapping improves slightly at small off-normal angles of incidence, agreeing with previous results on nano-pore PC structures.[47–49]

Conflicts of interest

There are no conflicts to declare.

Acknowledgements

This work was supported by the Ontario Research Fund and the Natural Sciences and Engineering Research Council of Canada.

References

1 A. Fujishima and K. Honda, *Nature*, 1972, **238**, 37–38.
2 N. Serpone, A. V. Emeline, V. K. Ryabchuk, V. N. Kuznetsov, Y. M. Artem'ev and S. Horikoshi, *ACS Energy Lett.*, 2016, **1**, 931–948.
3 M. R. Hoffmann, S. T. Martin, W. Choi and D. W. Bahnemann, *Chem. Rev.*, 1995, **95**, 69–96.
4 T. Rajh, N. M. Dimitrijevic, M. Bissonnette, T. Koritarov and V. Konda, *Chem. Rev.*, 2014, **114**, 10177–10216.
5 Y. Gai, J. Li, S.-S. Li, J.-B. Xia and S.-H. Wei, *Phys. Rev. Lett.*, 2009, **102**, 036402.
6 M. Radecka, M. Rekas, A. Trenczek-Zajac and K. Zakrzewska, *J. Power Sources*, 2008, **181**, 46–55.
7 S. John, *Phys. Rev. Lett.*, 1987, **58**, 2486–2489.
8 J. I. L. Chen, G. von Freymann, S. Y. Choi, V. Kitaev and G. A. Ozin, *Adv. Mater.*, 2006, **18**, 1915–1919.
9 X. Chen, J. Ye, S. Ouyang, T. Kako, Z. Li and Z. Zou, *ACS Nano*, 2011, **5**, 4310–4318.
10 M. Wu, J. Jin, J. Liu, Z. Deng, Y. Li, O. Deparis and B.-L. Su, *J. Mater. Chem. A*, 2013, **1**, 15491–15500.
11 V. Jovic, H. Idriss and G. I. N. Waterhouse, *Chem. Phys.*, 2016, **479**, 109–121.
12 R. Mitchell, R. Brydson and R. E. Douthwaite, *Phys. Chem. Chem. Phys.*, 2015, **17**, 493–499.
13 J. Liu, H. Zhao, M. Wu, B. Van der Schueren, Y. Li, O. Deparis, J. Ye, G. A. Ozin, T. Hasan and B.-L. Su, *Adv. Mater.*, 2017, **29**, 1605349.
14 J. Liu, J. Jin, Y. Li, H.-W. Huang, C. Wang, M. Wu, L.-H. Chen and B.-L. Su, *J. Mater. Chem. A*, 2014, **2**, 5051–5059.
15 M. El Harakeh and L. Halaoui, *J. Phys. Chem. C*, 2010, **114**, 2806–2813.
16 S. Bayram and L. Halaoui, *Part. Part. Syst. Charact.*, 2013, **30**, 706–714.
17 H. Zhao, Z. Hu, J. Liu, Y. Li, M. Wu, G. Van Tendeloo and B.-L. Su, *Nano Energy*, 2018, **47**, 266–274.
18 O. Deparis, S. R. Mouchet and B.-L. Su, *Phys. Chem. Chem. Phys.*, 2015, **17**, 30525–30532.
19 M. Curti, J. Schneider, D. W. Bahnemann and C. B. Mendive, *J. Phys. Chem. Lett.*, 2015, **6**, 3903–3910.
20 V. Likodimos, *Appl. Catal., B*, 2018, **230**, 269–303.
21 P. Jiang, J. F. Bertone, K. S. Hwang and V. L. Colvin, *Chem. Mater.*, 1999, **11**, 2132–2140.
22 S. H. Park and Y. Xia, *Langmuir*, 1999, **15**, 266–273.
23 J. I. L. Chen and G. A. Ozin, *J. Mater. Chem.*, 2009, **19**, 2675–2678.
24 E. Eftekhari, P. Broisson, N. Aravindakshan, Z. Wu, I. S. Cole, X. Li, D. Zhao and Q. Li, *J. Mater. Chem. A*, 2017, **5**, 12803–12810.
25 M. Xu, Y. Gao, E. M. Moreno, M. Kunst, M. Muhler, Y. Wang, H. Idriss and C. Wöll, *Phys. Rev. Lett.*, 2011, **106**, 138302.
26 T. Luttrell, S. Halpegamage, J. Tao, A. Kramer, E. Sutter and M. Batzill, *Sci. Rep.*, 2014, **4**, 4043.
27 N. Hosaka, T. Sekiya, C. Satoko and S. Kurita, *J. Phys. Soc. Jpn.*, 1997, **66**, 877–880.

28 A. Chutinan and S. John, *Phys. Rev. A: At., Mol., Opt. Phys.*, 2008, **78**, 023825.
29 X. Zhang and S. John, *Phys. Rev. B*, 2019, **99**, 035417.
30 A. L. Linsebigler, G. Lu and J. T. Yates, *Chem. Rev.*, 1995, **95**, 735–758.
31 J. E. G. J. Wijnhoven and W. L. Vos, *Science*, 1998, **281**, 802–804.
32 O. D. Velev and E. W. Kaler, *Adv. Mater.*, 2000, **12**, 531–534.
33 A. Richel, N. P. Johnson and D. W. McComb, *Appl. Phys. Lett.*, 2000, **76**, 1816–1818.
34 J. E. G. J. Wijnhoven, L. Bechger and W. L. Vos, *Chem. Mater.*, 2001, **13**, 4486–4499.
35 J. W. Galusha, C.-K. Tsung, G. D. Stucky and M. H. Bartl, *Chem. Mater.*, 2008, **20**, 4925–4930.
36 A. Blanco, E. Chomski, S. Grabtchak, M. Ibisate, S. John, S. W. Leonard, C. Lopez, F. Meseguer, H. Miguez, J. P. Mondia, G. A. Ozin, O. Toader and H. M. van Driel, *Nature*, 2000, **405**, 437–440.
37 F. García-Santamaría, M. Ibisate, I. Rodríguez, F. Meseguer and C. López, *Adv. Mater.*, 2003, **15**, 788–792.
38 J. S. King, E. Graugnard and C. J. Summers, *Adv. Mater.*, 2005, **17**, 1010–1013.
39 E. Graugnard, J. S. King, D. P. Gaillot and C. J. Summers, *Adv. Funct. Mater.*, 2006, **16**, 1187–1196.
40 P. V. Braun and P. Wiltzius, *Adv. Mater.*, 2001, **13**, 482–485.
41 K. Busch and S. John, *Phys. Rev. E: Stat., Nonlinear, Soft Matter Phys.*, 1998, **58**, 3896–3908.
42 J. Liu, G. Liu, M. Li, W. Shen, Z. Liu, J. Wang, J. Zhao, L. Jiang and Y. Song, *Energy Environ. Sci.*, 2010, **3**, 1503–1506.
43 Y. G. Seo, K. Woo, J. Kim, H. Lee and W. Lee, *Adv. Funct. Mater.*, 2011, **21**, 3094–3103.
44 D. Qi, L. Lu, Z. Xi, L. Wang and J. Zhang, *Appl. Catal., B*, 2014, **160–161**, 621–628.
45 Z. Cai, Z. Xiong, X. Lu and J. Teng, *J. Mater. Chem. A*, 2014, **2**, 545–553.
46 C. Cheng, S. K. Karuturi, L. Liu, J. Liu, H. Li, L. T. Su, A. I. Y. Tok and H. J. Fan, *Small*, 2012, **8**, 37–42.
47 S. Eyderman, S. John and A. Deinega, *J. Appl. Phys.*, 2013, **113**, 154315.
48 K. Q. Le and S. John, *Opt. Express*, 2014, **22**, A1–A12.
49 M.-L. Hsieh, A. Kaiser, S. Bhattacharya, S. John and S.-Y. Lin, *Sci. Rep.*, 2020, **10**, 11857.